

Caspase-3-Responsive Dual-Enhanced $^1\text{H}/^{19}\text{F}$ MRI Bimodal Probe for *In Vivo* Tumor Apoptosis Imaging

Yue Zhu,^{||} Lei Zhang,^{||} Sha Li, Yingying Luo, Long Xiao, Qiao Yu, Zhong-Xing Jiang, Xin Zhou,* and Shizhen Chen*



Cite This: <https://doi.org/10.1021/acs.analchem.4c06853>



Read Online

ACCESS |



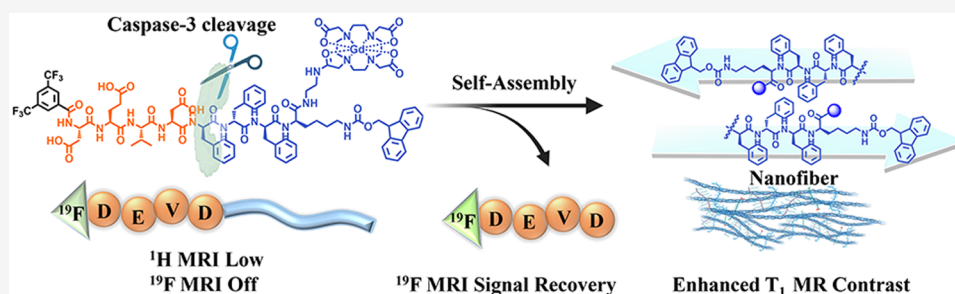
Metrics & More



Article Recommendations



Supporting Information



ABSTRACT: Caspase-3 (Cas-3) is a crucial cysteine protease involved in executing cell apoptosis, a process that is a hallmark of tumor cell apoptosis response to chemotherapy. Developing molecular imaging probes that specifically detect apoptotic signals during tumor treatment is considered to be one of the most important and effective strategies for reducing cancer-associated death rates and improving treatment outcomes. However, achieving a dual-enhanced bimodal probe in a single molecule remains a significant challenge. In this study, we developed a $^1\text{H}/^{19}\text{F}$ dual-enhanced magnetic resonance imaging (MRI) probe, $\text{CF}_3\text{DEVDFFFK}(\text{Fmoc})\text{-Gd}$, responsive to caspase-3 for *in vivo* imaging of apoptotic cells. Upon interaction with caspase-3, $\text{CF}_3\text{DEVDFFFK}(\text{Fmoc})\text{-Gd}$ efficiently splits into two components CF_3DEV and $\text{FFFK}(\text{Fmoc})\text{-C}_2\text{-Gd}$, where $\text{FFFK}(\text{Fmoc})\text{-C}_2\text{-Gd}$ subsequently self-assembles into nanofibers. This process activates both ^{19}F MRI and ^1H MRI, with longitudinal relaxivity (r_1) increasing from 9.38 ± 0.22 to $23.24 \pm 2.33 \text{ mM}^{-1} \text{ s}^{-1}$ at 0.5 T and turning on the ^{19}F MRI signal due to the absence of the paramagnetic relaxation enhancement (PRE) effect. *In vivo* imaging results demonstrated that, after systemic administration, $\text{CF}_3\text{DEVDFFFK}(\text{Fmoc})\text{-Gd}$ effectively accumulated in apoptotic 4T1 tumor tissues, resulting in significantly enhanced ^1H MRI signals for visualization of caspase-3 activity in doxorubicin-treated apoptotic 4T1 tumor tissues, with signal intensity three times greater than that of Gd-DTPA. ^{19}F MRI further complemented ^1H MRI, with a notable recovery of the ^{19}F MRI signal after intratumoral injection. These results confirm that $\text{CF}_3\text{DEVDFFFK}(\text{Fmoc})\text{-Gd}$ effectively reports tumor apoptosis through combined ^1H and ^{19}F MRI, offering a promising approach for the preliminary assessment of antitumor efficacy *in vivo*.

INTRODUCTION

As an indispensable cysteine protease responsible for apoptosis, caspase-3 is a distinctive biomarker of programmed cell death.^{1,2} Tumor heterogeneity leads to variability in chemotherapy response, underscoring the importance of detecting caspase-3 activity and localization of apoptosis in tumors to assess early treatment efficacy.^{3–5} Monitoring caspase-3 activity not only aids in evaluation but also provides valuable insights for refining tumor treatment strategies and preclinical screening of anticancer drugs. In recent years, various molecular imaging probes have been developed for the noninvasive detection of caspase-3 activity in apoptotic tumor tissue, using imaging modalities such as fluorescence (FL), photoacoustic (PA), positron emission tomography (PET), and MRI.^{6–11} While fluorescence imaging is constrained by limited penetration depth and spatial resolution due to light absorption and scattering, PET tracers face challenges related

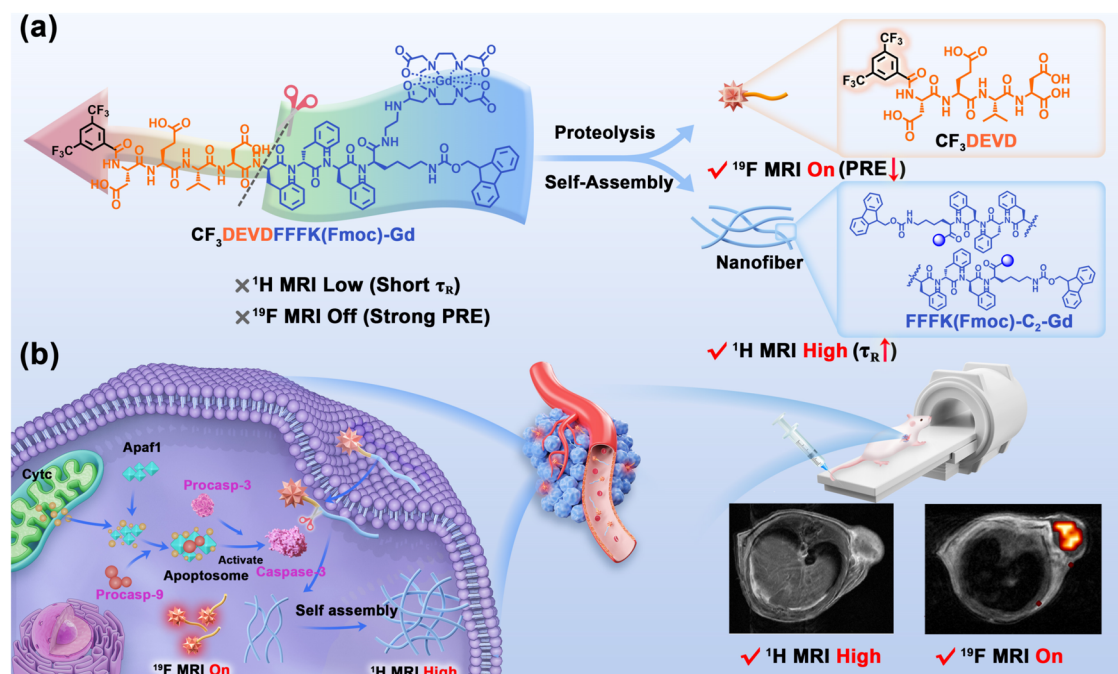
to radiation and spatial resolution that hinder their ability to pinpoint specific apoptotic regions in tumors. In contrast, MRI provides three-dimensional anatomical images of the target area, facilitating a more intuitive visualization of the tumor site.

MRI is a widely used noninvasive medical imaging technique in clinical applications.^{12–15} Recently, there has been increasing interest in utilizing MRI for the molecular imaging of biomolecules, necessitating the development of specialized MRI probes.¹⁶ Researchers have successfully identified various endogenous substances *in vivo* by modifying Gd(III)-based

Received: December 17, 2024

Revised: April 13, 2025

Accepted: April 15, 2025

Scheme 1. Design Principle of a Caspase-3-Responsive $^1\text{H}/^{19}\text{F}$ MRI Dual-Modality Probe^a

^a(a) Chemical structure of the probe and the response process: $\text{CF}_3\text{DEVDFFFK}(\text{Fmoc})\text{-Gd}$ is cleaved into two parts by caspase-3, and then $\text{FFFK}(\text{Fmoc})\text{-C}_2\text{-Gd}$ self-assembles into nanofibers *in situ*. (b) Schematic representation of $\text{CF}_3\text{DEVDFFFK}(\text{Fmoc})\text{-Gd}$ for $^1\text{H}/^{19}\text{F}$ MR imaging of caspase-3 activity in apoptotic tumor cells.

probes. Besides, ^{19}F has emerged as a promising MRI nuclide due to its favorable gyromagnetic ratio (γ) of 40.05 MHz/T and a broad range of chemical shifts (>350 ppm). Mainly, ^{19}F exhibits a 100% natural isotope abundance ratio and minimal biodistribution ($<10^{-6}$ M, restricted to bone and teeth).^{17–21} Leveraging the proximity of γ values between ^1H and ^{19}F , ^{19}F MRI can be used with most ^1H MRI instruments by adjusting the hardware such as the radio frequency (RF) coil, which significantly reduces dual-mode imaging requirements and costs. ^{19}F MRI is a hot spot imaging modality with a unique advantage: it is unaffected by background signals, which makes it an invaluable complement to ^1H MRI.^{22,23} Functional ^{19}F MRI probes are useful for *in vivo* molecular detection and cell tracking/tracing, and tumor marker identification.^{24–28} Activatable multimodal probes that show the enhancement of multiplex imaging signals upon interaction with their specific molecular target have become powerful tools for rapid and precise imaging of biological processes. Several dual-modality probes have been developed to detect caspase-3 activity, including FL/MRI, PA/MRI, and FL/PA.^{29–31} Therefore, the exploration of caspase-3-responsive multimodal probes holds significant research potential. While conventional ^1H MRI excels in delivering high-resolution anatomical visualization, its utility in biomarker tracking remains constrained by low intrinsic contrast due to the ubiquitous water content in biological tissues.³² ^{19}F MRI with negligible endogenous background interference enables highly sensitive detection of biomolecular targets and has drawn extensive attention from the biomedical research community recently. However, this modality exclusively detects exogenous ^{19}F -containing probes, limiting its capacity to provide a comprehensive biological context. $^1\text{H}/^{19}\text{F}$ MRI dual-modal imaging is expected to compensate for the limitations of single-modal imaging and accomplish synergistic morphological and physiological imag-

ing.^{33–35} Notably, this dual-modality imaging can be performed with the same instrument, eliminating the challenges associated with differences in contrast injection dosage and detection sensitivity between different imaging modalities.

A dual-enhanced probe $\text{CF}_3\text{DEVDFFFK}(\text{Fmoc})\text{-Gd}$ was developed to detect caspase-3 using $^1\text{H}/^{19}\text{F}$ MRI. Under normal conditions, the ^{19}F signal of the probe remained inactive due to the PRE effect. In an environment where caspase-3 is overexpressed, the DEVD sequence cleaves, forming CF_3DEVD and $\text{FFFK}(\text{Fmoc})\text{-C}_2\text{-Gd}$ segments. Systemic studies demonstrate that the incorporation of additional phenylalanine and Fmoc groups on lysine could accelerate the assembly rate due to the highly hydrophobic environment. This activates the ^{19}F signal and triggers *in situ* self-assembly of the $\text{FFFK}(\text{Fmoc})\text{-C}_2\text{-Gd}$ portion that accumulates at the tumor site with T_1 decreased subsequently due to a longer rotational correlation time (τ_R). Simultaneous enhancement of ^{19}F and ^1H signals allowed the noninvasive detection of caspase, facilitating early assessment of the therapeutic effects on tumors. ^1H MRI provides anatomical images of tumor tissue and ^{19}F MRI provides “hot spot” imaging with a high signal-to-background ratio (SBR), effectively complementing the information provided by ^1H MRI (Scheme 1).

EXPERIMENTAL SECTION

Reagents. The source for the reagents is described in the Supporting Information. The $\text{CF}_3\text{DEVDFFFK}(\text{Fmoc})\text{-Gd}$ was synthesized using a solid-phase synthetic method. The detailed procedure and characterization data are described in the Supporting Information (Scheme S3).

Measurement of the Longitudinal and Transverse Relaxivities (r_1 and r_2). To measure the r_1 and r_2 of FF-C_n-

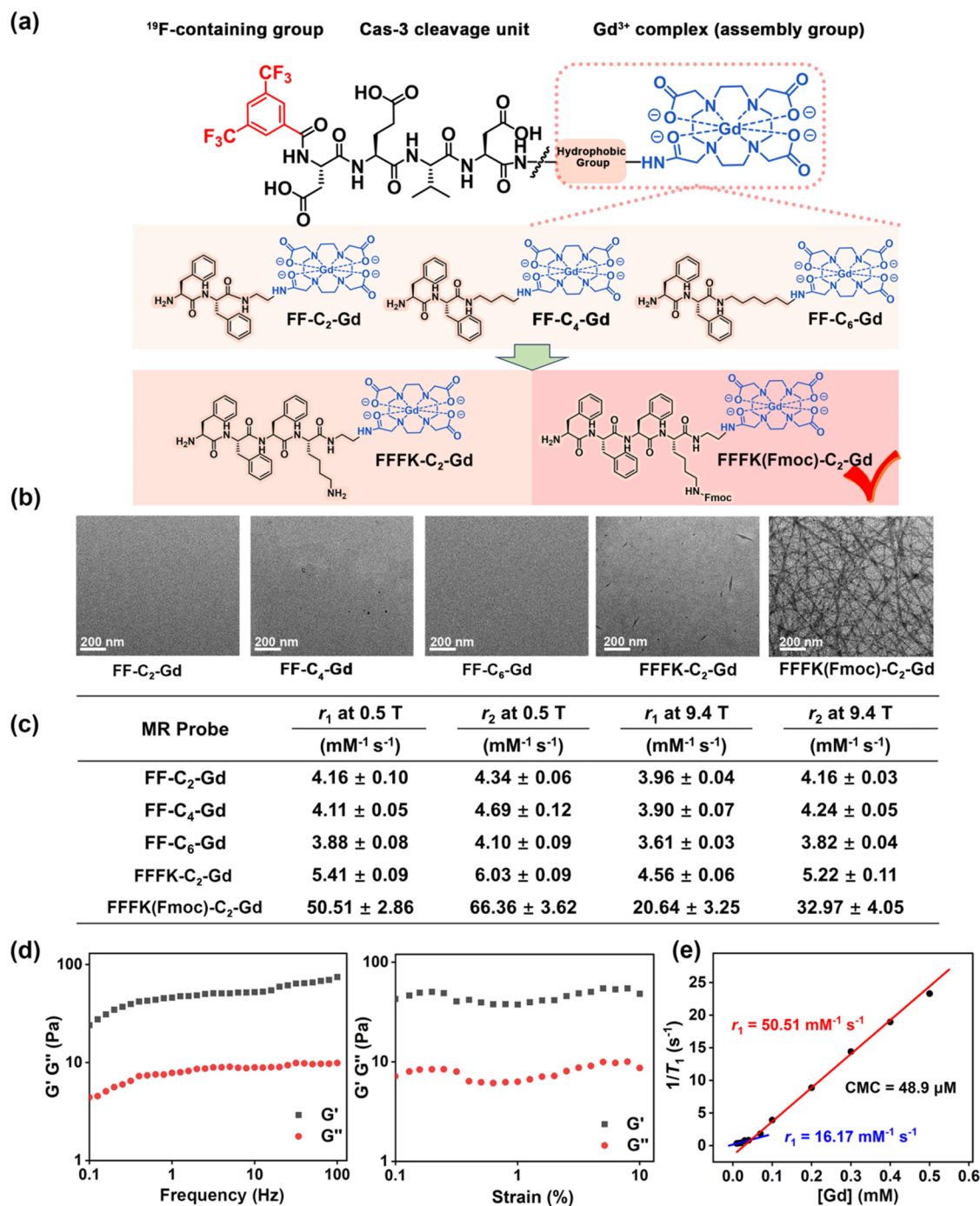


Figure 1. Optimization and characterization of self-assembling molecules. (a) Chemical structures of Gd-based MR probes. (b) TEM images of the probes (100 μ M). Scale bar = 200 nm. (c) Longitudinal and transverse relaxivities of the probes at 0.5 and 9.4 T NMR (37 $^{\circ}$ C). (d) Dynamic frequency of the storage modulus (G' , black) and the loss modulus (G'' , red) of FFFK(Fmoc)-C₂-Gd at a strain of 1.0% at 25 $^{\circ}$ C. (e) CMC of FFFK(Fmoc)-C₂-Gd in Tris buffer (pH 7.4, 0.5 T). Longitudinal relaxivity below 0.07 mM Gd concentration (blue). Longitudinal relaxivity above 0.07 mM Gd concentration (red). Data are presented as the mean \pm SD ($n = 3$).

Gd, CF₃DEVDFFFK(Fmoc)-Gd, CF₃DEVDC₂-Gd, or FFFK(Fmoc)-C₂-Gd, a series of Tris buffers containing 0.02, 0.2, 0.4, and 1.0 mM compounds were prepared. To evaluate the r_1 and r_2 of CF₃DEVDFFFK(Fmoc)-Gd or CF₃DEVDC₂-Gd toward caspase-3 at 0.5 and 9.4 T, CF₃DEVDFFFK(Fmoc)-Gd or CF₃DEVDC₂-Gd was incubated with caspase-3 (5 μ g mL⁻¹) in Tris buffer at 37 $^{\circ}$ C for 120 min and the T_1 and T_2 value in each solution were then acquired by a series of inversion-prepared fast spin-echo scans on the 0.5 T NMR

relaxometer (Bruker, Germany) and 9.4 T spectrometer (Bruker, Germany). The r_1 of FFFK(Fmoc)-C₂-Gd was acquired by a series of inversion-prepared fast spin-echo scans on the 0.5 T NMR relaxometry (Bruker, Germany) and 9.4 T spectrometers (Bruker, Germany) without incubated caspase-3. Longitudinal and transverse relaxivities (r_1 and r_2) were determined as $1/T_1$ and $1/T_2$, which were plotted versus the concentrations of each probe. The plot was fitted by linear regression, and the longitudinal relaxivities (r_1 , unit of mM⁻¹

s^{-1}) and transverse relaxation rate (r_2 , unit of $\text{mM}^{-1} \text{s}^{-1}$) were calculated based on the slope of each plot.

In Vitro $^1\text{H}/^{19}\text{F}$ MRI. ^1H T_1 -weighted MRI and ^{19}F MRI of the solution were performed on the 9.4 T imaging system (Bruker Avance 400, Germany). $\text{CF}_3\text{DEVDFFFK}(\text{Fmoc})\text{-Gd}$ ($200 \mu\text{M}$) was incubated with caspase-3 ($5.0 \mu\text{g mL}^{-1}$) in Tris buffer at 37°C for different times (0, 20, 60, 120, 240 min), ^1H T_1 -weighted MRI of different samples was performed with a rapid acquisition with refocused echoes (RARE) sequence. The parameters were set as follows: repetition time (TR) = 800 ms, echo time (TE) = 10 ms, the field of view (FOV) = $3 \text{ cm} \times 3 \text{ cm}$, slice thickness (SI) = 1 mm, rare factor = 4, matrix size = 256×256 . $\text{CF}_3\text{DEVDFFFK}(\text{Fmoc})\text{-Gd}$ (3.0 mM) was incubated with caspase-3 ($5.0 \mu\text{g mL}^{-1}$) in Tris buffer at 37°C for different times (0, 20, 60, 120, 240 min). ^{19}F MR imaging was acquired using a RARE sequence. The parameters were set as follows: TR = 4000 ms, TE = 3 ms, rare factor = 4, matrix size = 32×32 , number of average = 64, FOV = $3 \text{ cm} \times 3 \text{ cm}$, SI = 20 mm.

Bimodality Imaging of Cell Pellets. 4T1 cells (1×10^7) were seeded onto cell culture dishes. After the cell grew to $\sim 90\%$ confluence, the medium was removed and 6 mL of fresh medium containing staurosporine ($2 \mu\text{M}$) was added to the dishes and incubated for 2 h and then incubated with $\text{CF}_3\text{DEVDFFFK}(\text{Fmoc})\text{-Gd}$ ($500 \mu\text{M}$) in fetal bovine serum (FBS)-free RPMI-1640 for different times (0, 2, 4, 6, 8, 16 h). Then, the cells were trypsinized and then collected after centrifugation at 1200 rpm for 3 min. ^1H MRI was acquired using a RARE sequence (TR/TE = 800/10 ms, the flip angle = 90° , the FOV = $30 \text{ mm} \times 30 \text{ mm}$, matrix size = 256×256 , slice thickness = 1.0 mm). A ^{19}F (376.5 MHz) coil with an inner diameter of 10 mm was used for RF transmission and reception. ^{19}F MR imaging was acquired using a RARE sequence. The parameters were set as follows: TR = 3000 ms, TE = 3 ms, rare factor = 4, matrix size = 64×64 , number of average = 128, FOV = $30 \text{ mm} \times 30 \text{ mm}$, SI = 10 mm, and bandwidth = 5400 Hz.

In Vivo $^1\text{H}/^{19}\text{F}$ MRI. For noninvasive MR imaging of caspase-3 activity in subcutaneous tumor models, 200 μL of saline solution containing 0.084 mmol/kg $\text{CF}_3\text{DEVDFFFK}(\text{Fmoc})\text{-Gd}$ (2% DMSO, 30% PEG-2000) $\text{CF}_3\text{DEVDC}_2\text{-Gd}$ or Gd-DTPA were *i.v.* injected into each mouse ($n = 3$). The ^1H MR imaging was acquired prior to probe injection (Pre) and at 10 min, 30 min, 60 min, 2, 4, 6, and 12 h post injection. All of the MR imaging experiments were conducted on a 9.4 T small animal MR spectrometer (Bruker, Germany). The mice were scanned in the tail-first prone position. ^1H MRI was acquired using a RARE sequence (TR/TE = 500/8 ms, flip angle = 90° , FOV = $40 \text{ mm} \times 40 \text{ mm}$, matrix size = 256×256 , SI = 1.0 mm).

^{19}F MR imaging was acquired using a RARE sequence. The parameters were set as follows: TR = 4000 ms, TE = 9.2 ms, rare factor = 4, matrix size = 40×40 , number of average = 256, FOV = $40 \text{ mm} \times 40 \text{ mm}$, SI = 25 mm, bandwidth = 5400 Hz. The mouse was scanned before and after intratumoral injection of 50 μL saline solution containing 0.3 mmol/kg $\text{CF}_3\text{DEVDFFFK}(\text{Fmoc})\text{-Gd}$ (2% DMSO, 30% PEG-2000).

Each experiment was conducted in three mice. Acquired MRI data were then transferred as DICOM images to a RadiAnt DICOM Viewer for quantitative image analysis. This consisted of manual segmentation of the tumor region of interest (ROI) for each slice, slice-wise normalization of mean tumor signal intensity with the pure water reference standard

to account for intersession variability, followed by combining these normalized, slice-wise values to generate mean volumetric tumor signal intensities (SI) for each time point. Percentage signal enhancement (%SE) was calculated at each time point as the % difference between the tumor SI in the precontrast data set: $\%SE(t) = (\text{SI}(t) - \text{SI}(t=0))/\text{SI}(t=0)$; for each mouse, for every session.

RESULTS AND DISCUSSION

Optimization of the Self-Assembling Unit. Diphenylalanine (FF), as the core recognition motif of Alzheimer's β -amyloid polypeptide, has attracted increasing attention due to its excellent assembly ability, simple structure, and ease of chemical derivatization.³⁶ In this study, a series of FF-containing complexes were designed and synthesized, including $\text{FF-C}_2\text{-Gd}$, $\text{FF-C}_4\text{-Gd}$, $\text{FF-C}_6\text{-Gd}$, $\text{FFFK-C}_2\text{-Gd}$, and $\text{FFFK}(\text{Fmoc})\text{-C}_2\text{-Gd}$ (Figure 1a). After the successful synthesis of these complexes (Schemes S1 and S2), we first focused on the study of their microstructures using transmission electron microscopy (TEM). The TEM results showed that typical well-ordered nanofibers of $\text{FFFK}(\text{Fmoc})\text{-C}_2\text{-Gd}$ with a width of $\approx 7 \text{ nm}$ were observed, whereas $\text{FF-C}_2\text{-Gd}$, $\text{FF-C}_4\text{-Gd}$, and $\text{FF-C}_6\text{-Gd}$ did not form nanostructures under the same condition and only a minimal presence of fibers was detected for $\text{FFFK-C}_2\text{-Gd}$ (Figure 1b). Furthermore, the longitudinal and transverse relaxants were investigated under various concentrations (Figure 1c). The complexes containing the carbon linker groups ($\text{FF-C}_2\text{-Gd}$, $\text{FF-C}_4\text{-Gd}$, $\text{FF-C}_6\text{-Gd}$) exhibited longitudinal relaxivities similar to those of Gd-DOTA at both 0.5 and 9.4 T, indicating a lack of self-assembly behavior under these conditions, probably due to the relatively hydrophilic environment provided by the Gd-DO3A moiety.³⁷ Notably, the addition of an extra phenylalanine residue to the scaffold did not significantly change the r_1 . To increase the hydrophobic environment in addition to FF, a further 9-fluorenylmethylloxycarbonyl (Fmoc) was subsequently attached to the compartment between FFF and Gd-DO3A. The resulting longitudinal relaxivity of $\text{FFFK}(\text{Fmoc})\text{-C}_2\text{-Gd}$ increased 10-fold compared to $\text{FFFK-C}_2\text{-Gd}$ at 0.5 T, attributed to the formation of fiber-like microstructure which limits the rotational correlation time to increase the relaxivity. In addition, the $\text{FFFK}(\text{Fmoc})\text{-C}_2\text{-Gd}$ complex tended to form a hydrogel in an aqueous solution, showing behavior similar to that of other phenylalanine-containing compounds.

As a signature parameter, dynamic strain scanning was performed to evaluate the viscoelasticity of the obtained $\text{FFFK}(\text{Fmoc})\text{-C}_2\text{-Gd}$ hydrogels and determine the optimal conditions for dynamic frequency scanning. The storage modulus (G') and loss modulus (G'') showed a weak dependence within the strain range from 0.1 to 100% for a 100 μM $\text{FFFK}(\text{Fmoc})\text{-C}_2\text{-Gd}$ gel, indicating the hydrogel nature of the sample, with G' dominating (Figure 1d). Setting the strain amplitude to 1.0% and using dynamic frequency sweeps revealed a slight increase in both G' and G'' values, increasing slightly as the frequency increased from 0.1 to 10 Hz. Throughout this range, G' remained approximately 8 times greater than G'' , indicating the resilience of the hydrogel to external shear forces.

To quantify the concentration-dependent aggregation of $\text{FFFK}(\text{Fmoc})\text{-C}_2\text{-Gd}$, its critical micelle concentration (CMC) was determined to be 55.2 μM by acquiring fluorescence spectra of $\text{FFFK}(\text{Fmoc})\text{-C}_2\text{-Gd}$ in aqueous solutions with

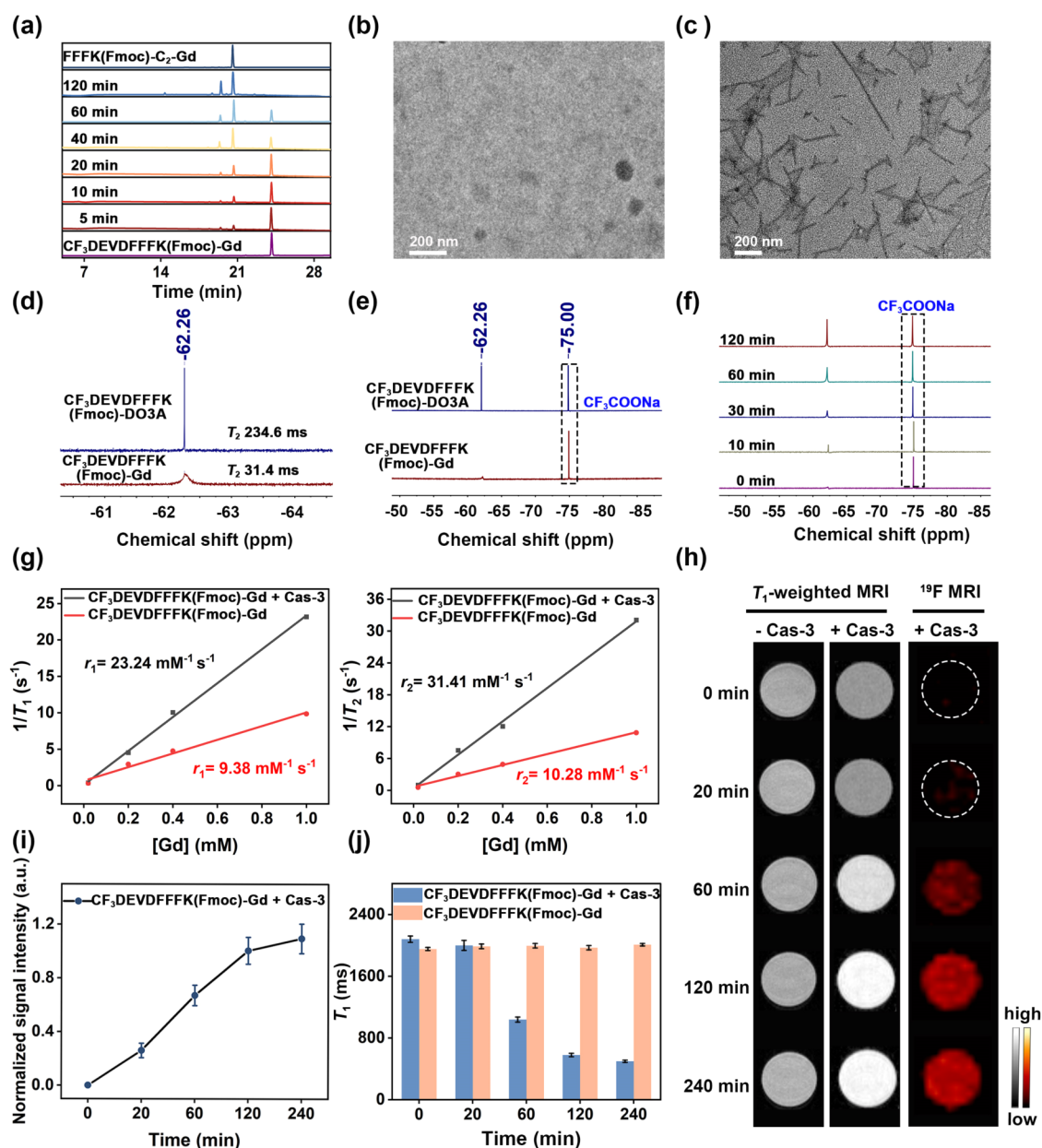


Figure 2. *In vitro* characterization of $\text{CF}_3\text{DEVDFFFK(Fmoc)-Gd}$. (a) HPLC traces of $\text{CF}_3\text{DEVDFFFK(Fmoc)-Gd}$ ($100 \mu\text{M}$) after incubation with caspase-3 ($5 \mu\text{g mL}^{-1}$) in Tris buffer (pH 7.4) at different times. (b) TEM images of $\text{CF}_3\text{DEVDFFFK(Fmoc)-Gd}$ ($100 \mu\text{M}$). Scale bar: 200 nm. (c) TEM images of $\text{CF}_3\text{DEVDFFFK(Fmoc)-Gd}$ ($100 \mu\text{M}$) after incubation with caspase-3 ($3 \mu\text{g mL}^{-1}$). Scale bar = 200 nm. (d) ^{19}F NMR spectra and T_2 values of ^{19}F in $\text{CF}_3\text{DEVDFFFK(Fmoc)-Gd}$ ($100 \mu\text{M}$) and $\text{CF}_3\text{DEVDFFFK(Fmoc)-DO3A}$ ($100 \mu\text{M}$) in Tris buffer (pH 7.4). (e) ^{19}F NMR spectra of $\text{CF}_3\text{DEVDFFFK(Fmoc)-Gd}$ ($100 \mu\text{M}$) and $\text{CF}_3\text{DEVDFFFK(Fmoc)-DO3A}$ ($100 \mu\text{M}$). Sodium trifluoroacetate was added as an internal standard (-75.00 ppm). (f) Time-dependent ^{19}F NMR spectra of $\text{CF}_3\text{DEVDFFFK(Fmoc)-Gd}$ ($100 \mu\text{M}$) with caspase-3 ($5 \mu\text{g mL}^{-1}$) at 37°C . (g) Plots of $1/T_1$ and $1/T_2$ vs Gd^{3+} concentration to determine the r_1 and r_2 of $\text{CF}_3\text{DEVDFFFK(Fmoc)-Gd}$ on 0.5 T at 37°C . (h) Time course of T_1 -weighted MRI and ^{19}F "hot spot" MRI of $\text{CF}_3\text{DEVDFFFK(Fmoc)-Gd}$ ($200 \mu\text{M}$) with or without caspase-3 ($5 \mu\text{g mL}^{-1}$) in Tris buffer (pH 7.4) at 9.4 T. (i) Normalized ^{19}F MRI signal intensity of $\text{CF}_3\text{DEVDFFFK(Fmoc)-Gd}$ incubated with or without caspase-3 for a different time. (j) T_1 of $\text{CF}_3\text{DEVDFFFK(Fmoc)-Gd}$ incubated with or without caspase-3 on 0.5 T at different times. Data are presented as mean \pm SD ($n = 3$).

pyrene (Figure S1). Furthermore, the mutation point of the $\text{FFFK(Fmoc)-C}_2\text{-Gd}$ assembly was measured by using the relaxation method. The CMC of $\text{FFFK(Fmoc)-C}_2\text{-Gd}$ was found to be $48.9 \mu\text{M}$ using r_1 and $58.6 \mu\text{M}$ using r_2 , as derived from the intersection of two linear fits (Figures 1e and S2). In summary, this assembled molecule ($\text{FFFK(Fmoc)-C}_2\text{-Gd}$) served as the backbone for the molecular design.

Characterizations of the $^1\text{H}/^{19}\text{F}$ MRI Bimodal Probe. $\text{CF}_3\text{DEVDFFFK(Fmoc)-Gd}$ was synthesized through the

classical solid-phase peptide method and purified via reversed-phase high-performance liquid chromatography (Scheme S3). The final compound and synthetic intermediates were confirmed through liquid chromatography, high-resolution mass spectrometry, and NMR spectroscopy (Figures S52–S69). The DEVDF sequence serves as the cleavage site for caspase-3, resulting in the formation of CF_3DEVDF and $\text{FFFK(Fmoc)-C}_2\text{-Gd}$ segments. The caspase-responsive self-assembly and corresponding ^{19}F MR signal switch behavior of

Table 1. Longitudinal and Transverse Relaxivities of Gd-Based MR Probes in This Study^a

MR probe	r_1 at 0.5 T	r_2 at 0.5 T	r_1 at 9.4 T	r_2 at 9.4 T
	(mM ⁻¹ s ⁻¹)			
CF ₃ DEVDFFFK(Fmoc)-Gd	9.38 ± 0.22	10.28 ± 0.28	7.33 ± 0.92	8.54 ± 0.97
CF ₃ DEVDFFFK(Fmoc)-Gd + Caspase-3 ^b	23.24 ± 2.33	31.41 ± 5.05	11.91 ± 1.05	13.11 ± 1.95
CF ₃ DEVDC ₂ -Gd	6.48 ± 0.63	7.57 ± 0.59	5.12 ± 0.40	5.92 ± 0.49
CF ₃ DEVDC ₂ -Gd ± Caspase-3	6.73 ± 0.74	8.28 ± 0.81	5.43 ± 1.37	6.24 ± 0.95
Gd-DTPA	3.75 ± 0.05	4.08 ± 0.12	4.15 ± 0.10	5.00 ± 0.22

^a T_1 and T_2 values (0.5 or 9.4 T) were measured in Tris buffer (pH 7.4) at 37 °C using an inversion recovery spin-echo sequence. The effective r_1 and r_2 were obtained by plotting $1/T_1$ and $1/T_2$ versus the Gd³⁺ concentration. All values are presented as mean ± standard deviation ($n = 3$).
^bCaspase-3 (5 μg mL⁻¹) was used for the reaction.

CF₃DEVDFFFK(Fmoc)-Gd were first studied *in vitro*. The cleavage was initially examined by using high-performance liquid chromatography (HPLC). As the caspase-3 concentration increased from 0.1 to 5.0 μg mL⁻¹, the conversion percentage of CF₃DEVDFFFK(Fmoc)-Gd steadily increased, achieving complete activation after a 2 h incubation when using 5.0 μg mL⁻¹ caspase-3 (Figure S3). Following incubation with caspase-3 (5 μg mL⁻¹), the HPLC peak intensity of CF₃DEVDFFFK(Fmoc)-Gd ($t_R = 24.8$ min) gradually decreased, while two new peaks corresponding to the cleavage products, FFFK(Fmoc)-C₂-Gd ($t_R = 20.9$ min) and CF₃DEVDC₂-Gd ($t_R = 19.6$ min), emerged with increasing incubation time (Figure 2a). Further relaxivity measurements confirmed that the limit of detection (LOD) for CF₃DEVDFFFK(Fmoc)-Gd was approximately 0.1 μg mL⁻¹ (Figure S4).

Next, we then turn our attention to the morphological transformation of CF₃DEVDFFFK(Fmoc)-Gd in response to caspase-3 using TEM. Upon incubation with caspase-3 (5 μg mL⁻¹), extensive long nanofibers formed, driven primarily by hydrophobic interactions and π - π stacking between the released peptide monomers (Figure 2b,c). Initially irregular aggregates of CF₃DEVDFFFK(Fmoc)-Gd transformed into well-defined nanofibers approximately 9 nm in width (Figure 2c), with the FFFK(Fmoc)-C₂-Gd nanofibers intertwining to create dense networks. After 8 h, the solution transitioned into a hydrogel state. The specificity and molecular stability of CF₃DEVDFFFK(Fmoc)-Gd toward caspase-3 were subsequently evaluated (Figures S5 and S6). The competition studies using HPLC, longitudinal relaxation time measurement, and ¹⁹F NMR experiments collectively confirmed that CF₃DEVDFFFK(Fmoc)-Gd demonstrated superior specificity for caspase-3 over other representative enzymes. Stability tests showed that CF₃DEVDFFFK(Fmoc)-Gd remained highly stable in RPMI-1640 culture medium (Figure S6) and showed resistance within a pH range of 3.0 to 9.0 (Figure S7).

Next, we focused on investigating the ¹⁹F NMR behavior of the complex in the presence of caspase-3. Due to the strong PRE effect induced by Gd ion, the ¹⁹F signal of CF₃DEVDFFFK(Fmoc)-Gd exhibited a shorter transverse relaxation time ($T_2 = 31.4$ ms) and a relatively low signal intensity. In contrast, uncomplexed CF₃DEVDFFFK(Fmoc)-DO3A retained a longer transverse relaxation time ($T_2 = 234.6$ ms) and a more distinct ¹⁹F NMR signal (Figure 2d). This effect was demonstrated in the one-dimensional ¹⁹F NMR spectra, where the peak intensity of CF₃DEVDFFFK(Fmoc)-Gd was significantly reduced and broadened compared to that of CF₃DEVDFFFK(Fmoc)-DO3A (Figure 2e). Upon treatment of CF₃DEVDFFFK(Fmoc)-Gd with caspase-3, the DEVDC₂ sequence was cleaved, resulting in the formation of

CF₃DEVDC₂ and FFFK(Fmoc)-C₂-Gd segments. The ¹⁹F NMR peak of CF₃DEVDC₂ at -62.26 ppm became sharper and more intense in a time-dependent manner (Figure 2f), indicating that the intramolecular paramagnetic effect from Gd³⁺ on ¹⁹F was decreased by the cleavage of the probe.

Moreover, both the longitudinal and transverse relaxivities of CF₃DEVDFFFK(Fmoc)-Gd showed significant enhancement after incubation with caspase-3 in Tris buffer (Figures 2g and S8). Specifically, following the caspase-3 response, the r_1 of CF₃DEVDFFFK(Fmoc)-Gd increased from 9.38 ± 0.22 to 23.24 ± 2.33 mM⁻¹ s⁻¹ at 0.5 T and from 7.33 ± 0.92 to 11.91 ± 1.05 mM⁻¹ s⁻¹ at 9.4 T. In contrast, the control molecule CF₃DEVDC₂-Gd showed no significant change in r_1 before and after caspase-3 incubation (Table 1). After caspase-3 activation, r_1 of CF₃DEVDC₂-Gd was 6.73 ± 0.74 mM⁻¹ s⁻¹ at 0.5 T and 37 °C, highlighting the crucial role of FFFK(Fmoc) in promoting molecular self-assembly. The introduction of Fmoc in the FFFK side chain enhances molecular rigidity through π - π stacking, thereby improving assembly capabilities and tissue retention time.

Notably, the change in transverse relaxivities (r_2) of CF₃DEVDFFFK(Fmoc)-Gd before and after caspase-3 activation was even more pronounced. The r_2 increased from 10.28 ± 0.28 to 31.41 ± 5.05 mM⁻¹ s⁻¹ at 0.5 T and from 8.54 ± 0.97 to 13.11 ± 1.95 mM⁻¹ s⁻¹ at 9.4 T following caspase-3 incubation. This transformation of the small molecule into a nanofiber form of FFFK(Fmoc)-C₂-Gd, characterized by increased hydrophobicity and rigidity, likely contributed to the further enhancement of r_1 after activation, consistent with predictions from the Solomon-Bloembergen-Morgan (SBM) theory.^{38,39} In addition, the cleavage behavior was also examined using ¹H and ¹⁹F MRI. After caspase-3 activation, the elevated r_1 of CF₃DEVDFFFK(Fmoc)-Gd in response to caspase-3 led to brighter T_1 -weighted MR images, with the T_1 significantly decreasing after 4 h of incubation (Figure 2h,j). And the T_2 -weighted MRI signal darkened considerably, accompanied by a 12-fold decrease in T_2 (Figure S9). The ¹⁹F MRI signal intensity increased in a time-dependent manner (Figure 2h,i). Even though the probe demonstrated trimodal imaging ability, T_1 -weighted MRI is often preferred due to its "bright" imaging mode, which enhances the visibility of target areas such as tumors. The subsequent studies were mainly focused on T_1 and ¹⁹F imaging.

Cellular Study of the Bimodal Probe upon Caspase-3 Activation. Encouraged by the above results, we investigated the MR bimodality imaging of caspase-3 activity in 4T1 cell pellets was investigated. Before using CF₃DEVDFFFK(Fmoc)-Gd to monitor caspase-3 activity in apoptotic tumor cells, the cytotoxic effects on tumor cells were initially assessed (Figure S10). The CCK8 results demonstrated that

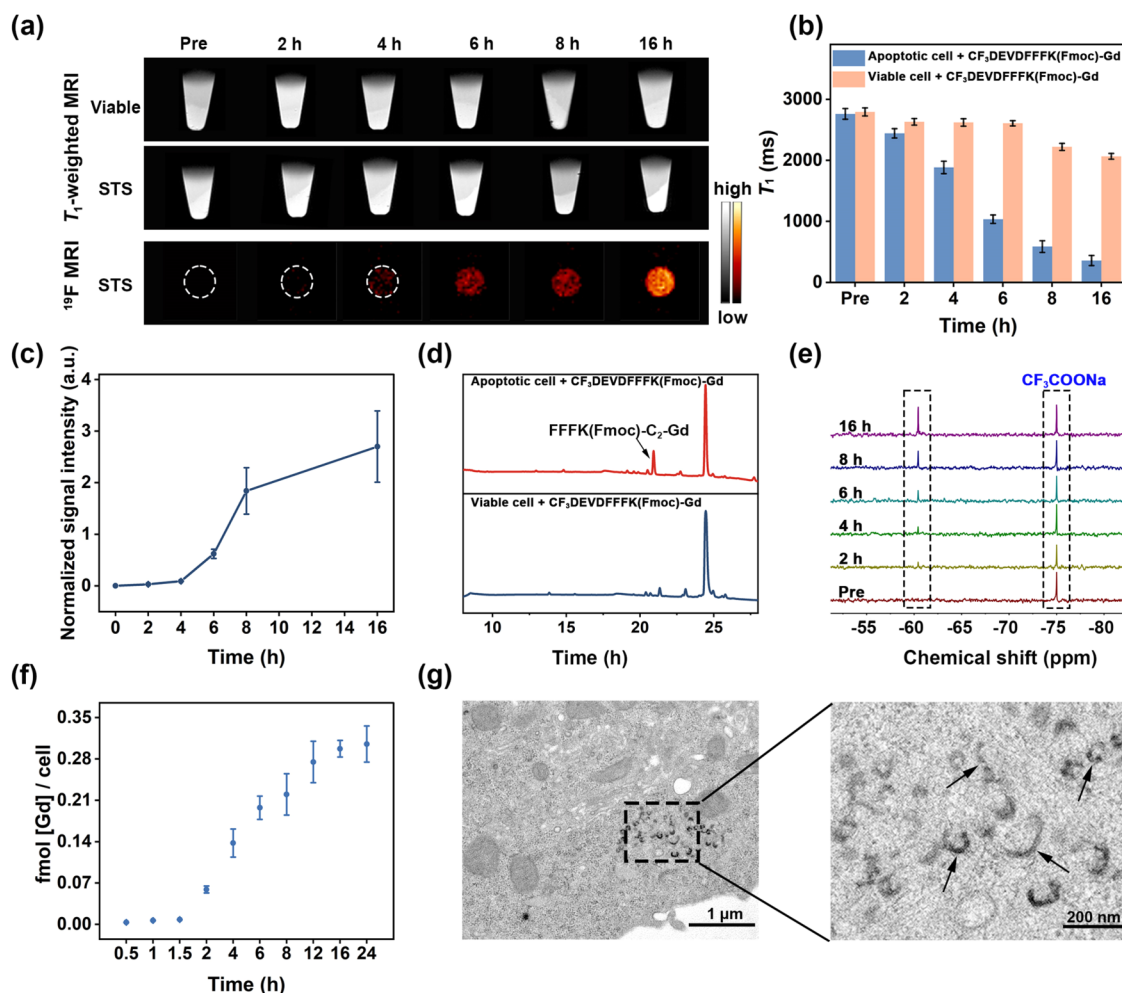


Figure 3. Cellular ^{19}F NMR/MRI and T_1 -weighted ^1H MRI. (a) Time-dependent T_1 -weighted MRI and ^{19}F “hot spot” MRI of STS-treated or untreated 4T1 cells incubated with $\text{CF}_3\text{DEVDFFFK(Fmoc)-Gd}$ at 9.4 T. (b) Time-dependent T_1 values of STS-treated or untreated 4T1 cells incubated with $\text{CF}_3\text{DEVDFFFK(Fmoc)-Gd}$ at 9.4 T. (c) Time-dependent normalized ^{19}F MRI signal intensity. (d) HPLC traces of $\text{CF}_3\text{DEVDFFFK(Fmoc)-Gd}$ incubated with viable cell lysates (blue), and apoptotic cell lysates (red) at 37 °C for 6 h. (e) Time-dependent ^{19}F NMR spectral change of STS-treated 4T1 cells incubated with $\text{CF}_3\text{DEVDFFFK(Fmoc)-Gd}$ at 9.4 T. (f) ICP-MS analysis of the Gd content in 4T1 cells after treatment with STS and $\text{CF}_3\text{DEVDFFFK(Fmoc)-Gd}$. (g) Low- and high-magnification TEM images of 4T1 cells treated with STS and $\text{CF}_3\text{DEVDFFFK(Fmoc)-Gd}$. Data are presented as mean \pm SD ($n = 3$).

$\text{CF}_3\text{DEVDFFFK(Fmoc)-Gd}$, $\text{CF}_3\text{DEVDC}_2\text{-Gd}$, and $\text{FFFK(Fmoc)-C}_2\text{-Gd}$ all exhibit high biocompatibility against 4T1 cells.

To establish an apoptotic tumor cell model, 4T1 cells were treated with staurosporine (STS), and the increased caspase-3 activity in these apoptotic cells was confirmed using the commercial caspase-3 fluorescent substrate Ac-DEVD-AMC (Figure S11). Next, $\text{CF}_3\text{DEVDFFFK(Fmoc)-Gd}$ (500 μM) in FBS-free RPMI-1640 was incubated with STS-induced apoptotic 4T1 cells for 8 h, and changes in the ^1H MRI signal of $\text{CF}_3\text{DEVDFFFK(Fmoc)-Gd}$ were monitored at various time points (Figure 3a). After 16 h of incubation, 4T1 cells treated with $\text{CF}_3\text{DEVDFFFK(Fmoc)-Gd}$ showed significantly brighter T_1 -weighted MRI compared to earlier time points. In contrast, the untreated STS group exhibited a remarkable reduction in T_1 and T_2 (Figures 3b and S12), indicating that $\text{CF}_3\text{DEVDFFFK(Fmoc)-Gd}$ undergoes specific assembly in response to caspase-3 in cells, leading to significant aggregation of $\text{FFFK(Fmoc)-C}_2\text{-Gd}$. The observed change in the ^1H MRI signal is likely due to the enhanced r_1 and the accumulation of nanofibers in 4T1 cells.

In addition, the ^{19}F MRI signal was first observed at 4 h, showing significant signal recovery that increased over time, correlating with the enhanced ^1H MRI signal and HPLC traces (Figure 3c–e). As the incubation time extended, the uptake of $\text{CF}_3\text{DEVDFFFK(Fmoc)-Gd}$ by the cells increased, reaching a plateau after 24 h (Figure 3f). The activation of the ^{19}F MRI signal provided a more intuitive method for observing the caspase-3 activity.

To explore the structural transformation of $\text{CF}_3\text{DEVDFFFK(Fmoc)-Gd}$ in response to caspase-3, STS-treated 4T1 cells were incubated with 500 μM $\text{CF}_3\text{DEVDFFFK(Fmoc)-Gd}$ for different durations, then collected and analyzed by TEM. Nanofibers with an average diameter of 11.3 ± 1.7 nm were observed in the cytoplasm of $\text{CF}_3\text{DEVDFFFK(Fmoc)-Gd}$ -treated cells after 8 h (Figure 3g). The enzymatic responsiveness of the probe *in vitro* may stem from the following structural limitations: 1. Steric hindrance: The bulky spatial obstruction between the DEVD cleavage site and the FFF self-assembly motif impedes the caspase-3 recognition and cleavage. Introducing flexible linkers (e.g., PEG or glycine spacers) between these domains could

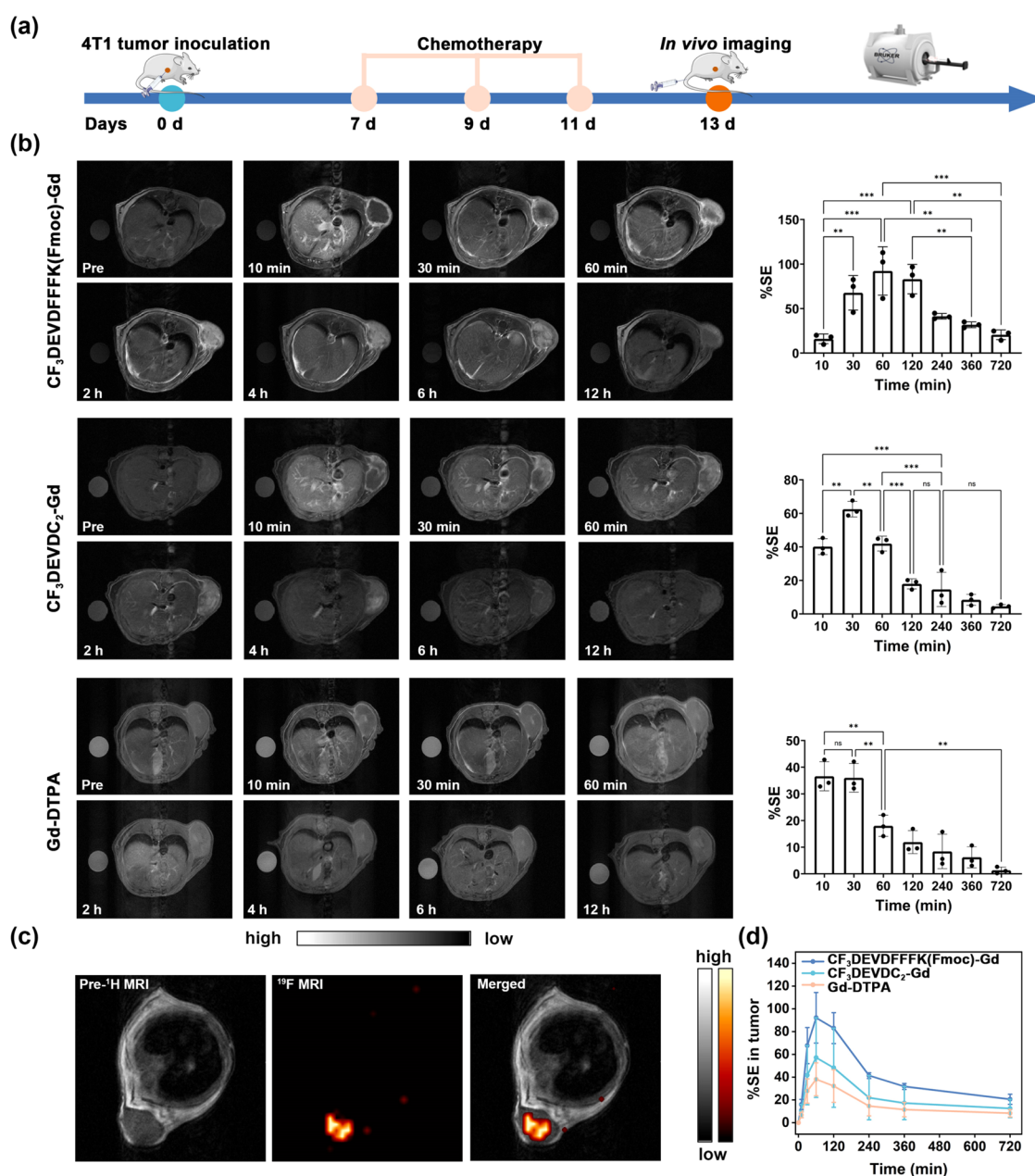


Figure 4. MR bimodal imaging of caspase-3 activity in apoptotic tumors in mice. (a) General schedule of animal experiments. (b) Representative T_1 -weighted MRI in tumors before (Pre), 10, 30, 60 min, 2, 4, 6, and 12 h after *i.v.* injection of $\text{CF}_3\text{DEVDFFK}(\text{Fmoc})\text{-Gd}$ ($0.084 \text{ mmol kg}^{-1}$). Values are expressed as the mean \pm SD ($n = 3$). Side circles indicate the pure water as the internal standard. (c) ^{19}F MRI of subcutaneous 4T1 tumor after intratumoral injection of $\text{CF}_3\text{DEVDFFK}(\text{Fmoc})\text{-Gd}$. (d) Quantification of %SE in tumors before (Pre), 10, 30, 60 min, 2, 4, 6, and 12 h post *i.v.* injection of $\text{CF}_3\text{DEVDFFK}(\text{Fmoc})\text{-Gd}$ ($0.084 \text{ mmol kg}^{-1}$). Data are presented as mean \pm SD ($n = 3$).

reduce steric hindrance. 2. Hydrophobicity-driven binding inhibition: The meta-trifluoromethylbenzoic acid group's rigidity and strong hydrophobicity likely compromise enzyme–substrate interactions. Replacing it with conformationally flexible fluorine-containing groups. 3. Suboptimal cellular membrane permeability: The probe's limited trans-membrane efficiency results in insufficient intracellular accumulation. Conjugation of cell-penetrating peptides could enhance cellular uptake.

***In Vivo* Bimodal Imaging of Tumor Apoptosis.** $\text{CF}_3\text{DEVDFFK}(\text{Fmoc})\text{-Gd}$ was administered to detect endogenous caspase-3 in subcutaneous 4T1 tumor-bearing mice using MRI (Figure 4a). This study established a tumor

apoptosis model, and increased caspase-3 activity in DOX-treated tumors was confirmed using Ac-DEVD-AMC (Figure S13). Two days after the final treatment with DOX or saline, mice were intravenously injected with $\text{CF}_3\text{DEVDFFK}(\text{Fmoc})\text{-Gd}$ ($0.084 \text{ mmol kg}^{-1}$). Following the tail vein injection of $\text{CF}_3\text{DEVDFFK}(\text{Fmoc})\text{-Gd}$, the probes circulated through the bloodstream, and within 10 min, noticeable signal enhancement was observed at the tumor boundary, with increased brightness (Figure 4b). After 2 h, both the $\text{CF}_3\text{DEVDFFK}(\text{Fmoc})\text{-Gd}$ and $\text{FFFK}(\text{Fmoc})\text{-C}_2\text{-Gd}$ had accumulated entirely at the tumor site, resulting in a maximum MR signal enhancement of approximately 96.2% (%SE, Figure 4d). The signal enhancement at the tumor site remained

around 24.1% at 12 h. In contrast, the MRI intensity of saline-treated tumors increased slightly, approximately 46.7% (Figures S14 and S15).

Furthermore, the initial distribution of $\text{CF}_3\text{DEVDC}_2\text{-Gd}$ ($0.084 \text{ mmol kg}^{-1}$) after injection was comparable to that of $\text{CF}_3\text{DEVDFFFK(Fmoc)-Gd}$ (Figure 4b). However, the MRI signal intensity peaked at 0.5 h and then rapidly declined, indicating metabolism without significant accumulation at the tumor site. This further supported the evidence that $\text{FFFK(Fmoc)-C}_2\text{-Gd}$ exhibited strong tissue retention after $\text{CF}_3\text{DEVDFFFK(Fmoc)-Gd}$ responded to caspase-3. Additionally, $\text{CF}_3\text{DEVDFFFK(Fmoc)-Gd}$ demonstrated higher relaxivity than Gd-DTPA, a commonly used clinical contrast agent, resulting in significantly improved image contrast after the same dose was administered. The peak signal at the tumor site occurred between 30 and 60 min post injection, followed by metabolic clearance. Analysis of Gd^{3+} ion content in various organs using ICP-MS, conducted 2 h after tail vein injection (Figures S16 and S17), showed that the $\text{CF}_3\text{DEVDFFFK(Fmoc)-Gd}$ group exhibited better tumor site accumulation compared to other organs, surpassing that of the $\text{CF}_3\text{DEVDC}_2\text{-Gd}$ and Gd-DTPA groups. ICP-MS results also identified the liver and kidneys as the primary organs responsible for metabolizing $\text{CF}_3\text{DEVDFFFK(Fmoc)-Gd}$. The *in vivo* half-life ($t_{1/2}$) of the probe was calculated as 91 min based on blood concentration data collected at multiple time points from normal mice (Figure S18). This result demonstrates rapid clearance of the probe from the bloodstream, which correlates with its high accumulation in the liver and kidneys (as evidenced by biodistribution studies), further confirming these organs as the primary sites for metabolic processing and systemic elimination. Two hours after intratumoral injection of $0.084 \text{ mmol kg}^{-1}$ $\text{CF}_3\text{DEVDFFFK(Fmoc)-Gd}$, the ^{19}F signal recovered significantly (Figure 4c). ^{19}F MRI confirmed the probe's response at the tumor site, making it suitable for quantitative monitoring. The systemic distribution of probe molecules following systemic administration results in significant dilution of the ^{19}F concentration at the tumor site. This challenge is further compounded by the enzyme-dependent activation mechanism, where ^{19}F imaging efficacy is constrained by both the local enzyme availability and probe concentration. To address these limitations, two strategic improvements are proposed: 1. Targeted probe design: Developing non-enzyme-responsive probes with active tumor-targeting moieties could enhance tumor-specific accumulation. 2. Fluorine payload optimization: Incorporating high-fluorine-density groups such as perfluoro-tert-butanol could amplify the ^{19}F signal intensity, potentially overcoming current sensitivity limitations. H&E staining of the main organs analysis across all groups exhibited no tissue damage (Figure S19).

CONCLUSIONS

In terms of molecular design, this probe achieves dual-enhanced MR signals through the EPR effect and *in situ* self-assembly strategies, demonstrating high relaxivity and superior signal-to-noise ratio (SNR) after enzymatic activation. The $^1\text{H}/^{19}\text{F}$ bimodal imaging provides a high spatial resolution and depth-independent detection capabilities. Notably, the Fmoc modification on the lysine side chain preserves the C-terminus as a functional site for conjugating additional moieties (e.g., fluorescent tags) to enable multimodal imaging, while addressing the limitations of earlier probes. This study presents

a novel strategy combining the enzyme-mediated PRE effect with an *in situ* self-assembly. The $^1\text{H}/^{19}\text{F}$ MRI dual-modality probe $\text{CF}_3\text{DEVDFFFK(Fmoc)-Gd}$ can provide information about the activity and distribution of caspase-3 in apoptotic tumor tissues of DOX-treated 4T1 tumor-bearing mice. The $\text{CF}_3\text{DEVDFFFK(Fmoc)-Gd}$ can efficiently split into two components including $\text{CF}_3\text{DEVDC}_2$ and $\text{FFFK(Fmoc)-C}_2\text{-Gd}$ in response to caspase-3, forming $\text{FFFK(Fmoc)-C}_2\text{-Gd}$ nanofibers, which enhance ^1H MRI signals and activate the ^{19}F signal. T_1 -weighted MRI of $\text{FFFK(Fmoc)-C}_2\text{-Gd}$ nanofibers provides a complete anatomical image of the tumor site and delineates the tumor boundary and the recovery of the ^{19}F MRI signal provides robust evidence for ^1H MRI. Compared to other dual-modal probes, $\text{CF}_3\text{DEVDFFFK(Fmoc)-Gd}$ can be used on a single MRI with $^1\text{H}/^{19}\text{F}$ coil, providing more convenient and faster sampling and better image matching. It is expected that the optimized probe can serve as a responsive *in situ* self-assembled scaffold to introduce other reactive responsive groups, thereby providing molecular imaging insights for relevant disease assessment by $^1\text{H}/^{19}\text{F}$ MRI.

ASSOCIATED CONTENT

Supporting Information

The Supporting Information is available free of charge at <https://pubs.acs.org/doi/10.1021/acs.analchem.4c06853>.

Synthetic routes of $\text{CF}_3\text{DEVDFFFK(Fmoc)-Gd}$ and $\text{CF}_3\text{DEVDC}_2\text{-Gd}$; NMR, MS, and HPLC of intermediates and products; ^{19}F spectra and HPLC spectra of $\text{CF}_3\text{DEVDFFFK(Fmoc)-Gd}$ mixed with caspase-3; ^{19}F responses of $\text{CF}_3\text{DEVDFFFK(Fmoc)-Gd}$ to various substances; observation of *in vivo* MRI in 4T1 model mice; and cytotoxicity of $\text{CF}_3\text{DEVDFFFK(Fmoc)-Gd}$ and $\text{CF}_3\text{DEVDC}_2\text{-Gd}$ (PDF)

AUTHOR INFORMATION

Corresponding Authors

Xin Zhou – State Key Laboratory of Magnetic Resonance Spectroscopy and Imaging, National Center for Magnetic Resonance in Wuhan, Wuhan Institute of Physics and Mathematics, Innovation Academy for Precision Measurement Science and Technology, Chinese Academy of Sciences-Wuhan National Laboratory for Optoelectronics, Huazhong University of Science and Technology, Wuhan 430071, P. R. China; University of Chinese Academy of Sciences, Beijing 100049, P. R. China; School of Biomedical Engineering, Hainan University, Sanya 572019, P. R. China; orcid.org/0000-0002-5580-7907; Email: xinzhou@wipm.ac.cn

Shizhen Chen – State Key Laboratory of Magnetic Resonance Spectroscopy and Imaging, National Center for Magnetic Resonance in Wuhan, Wuhan Institute of Physics and Mathematics, Innovation Academy for Precision Measurement Science and Technology, Chinese Academy of Sciences-Wuhan National Laboratory for Optoelectronics, Huazhong University of Science and Technology, Wuhan 430071, P. R. China; University of Chinese Academy of Sciences, Beijing 100049, P. R. China; School of Biomedical Engineering, Hainan University, Sanya 572019, P. R. China; Email: chenshizhen@wipm.ac.cn

Authors

Yue Zhu – State Key Laboratory of Magnetic Resonance Spectroscopy and Imaging, National Center for Magnetic Resonance in Wuhan, Wuhan Institute of Physics and Mathematics, Innovation Academy for Precision Measurement Science and Technology, Chinese Academy of Sciences-Wuhan National Laboratory for Optoelectronics, Huazhong University of Science and Technology, Wuhan 430071, P. R. China; University of Chinese Academy of Sciences, Beijing 100049, P. R. China

Lei Zhang – State Key Laboratory of Magnetic Resonance Spectroscopy and Imaging, National Center for Magnetic Resonance in Wuhan, Wuhan Institute of Physics and Mathematics, Innovation Academy for Precision Measurement Science and Technology, Chinese Academy of Sciences-Wuhan National Laboratory for Optoelectronics, Huazhong University of Science and Technology, Wuhan 430071, P. R. China; University of Chinese Academy of Sciences, Beijing 100049, P. R. China

Sha Li – State Key Laboratory of Magnetic Resonance Spectroscopy and Imaging, National Center for Magnetic Resonance in Wuhan, Wuhan Institute of Physics and Mathematics, Innovation Academy for Precision Measurement Science and Technology, Chinese Academy of Sciences-Wuhan National Laboratory for Optoelectronics, Huazhong University of Science and Technology, Wuhan 430071, P. R. China; University of Chinese Academy of Sciences, Beijing 100049, P. R. China

Yingying Luo – State Key Laboratory of Magnetic Resonance Spectroscopy and Imaging, National Center for Magnetic Resonance in Wuhan, Wuhan Institute of Physics and Mathematics, Innovation Academy for Precision Measurement Science and Technology, Chinese Academy of Sciences-Wuhan National Laboratory for Optoelectronics, Huazhong University of Science and Technology, Wuhan 430071, P. R. China; University of Chinese Academy of Sciences, Beijing 100049, P. R. China

Long Xiao – State Key Laboratory of Magnetic Resonance Spectroscopy and Imaging, National Center for Magnetic Resonance in Wuhan, Wuhan Institute of Physics and Mathematics, Innovation Academy for Precision Measurement Science and Technology, Chinese Academy of Sciences-Wuhan National Laboratory for Optoelectronics, Huazhong University of Science and Technology, Wuhan 430071, P. R. China

Qiao Yu – State Key Laboratory of Magnetic Resonance Spectroscopy and Imaging, National Center for Magnetic Resonance in Wuhan, Wuhan Institute of Physics and Mathematics, Innovation Academy for Precision Measurement Science and Technology, Chinese Academy of Sciences-Wuhan National Laboratory for Optoelectronics, Huazhong University of Science and Technology, Wuhan 430071, P. R. China

Zhong-Xing Jiang – State Key Laboratory of Magnetic Resonance Spectroscopy and Imaging, National Center for Magnetic Resonance in Wuhan, Wuhan Institute of Physics and Mathematics, Innovation Academy for Precision Measurement Science and Technology, Chinese Academy of Sciences-Wuhan National Laboratory for Optoelectronics, Huazhong University of Science and Technology, Wuhan 430071, P. R. China; University of Chinese Academy of Sciences, Beijing 100049, P. R. China; orcid.org/0000-0003-2601-4366

Complete contact information is available at:
<https://pubs.acs.org/10.1021/acs.analchem.4c06853>

Author Contributions

^{||}Y.Z. and L.Z. contributed equally to this work. All authors have approved the final version of the manuscript.

Notes

The authors declare no competing financial interest.

ACKNOWLEDGMENTS

This work was supported by the National Natural Science Foundation of China (U21A20392, 82127802, 22404064, 82102125), the Hubei Provincial Natural Science Foundation of China (2023BCB092, 2023AFB738), and CAS Youth Interdisciplinary Team (JCTD-2022-13).

REFERENCES

- (1) Salvesen, G. S. *Essays Biochem.* **2002**, *38*, 9–19.
- (2) Stennicke, H. R.; Salvesen, G. S. *Biochim. Biophys. Acta, Protein Struct. Mol. Enzymol.* **1998**, *1387* (1–2), 17–31.
- (3) Palmer, M.; Shen, B.; Jeon, J.; Lin, J.; Chin, F. T.; Rao, J. J. *Nucl. Med.* **2015**, *56* (9), 1415–1421.
- (4) Nguyen, Q.-D.; Smith, G.; Glaser, M.; Perumal, M.; Årstad, E.; Aboagye, E. O. *Proc. Natl. Acad. Sci. U.S.A.* **2009**, *106* (38), 16375–16380.
- (5) Wang, H.; Zhang, Q.; Chu, X.; Chen, T.; Ge, J.; Yu, R. *Angew. Chem., Int. Ed.* **2011**, *50* (31), 7065–7069.
- (6) Wang, Y.; Hu, X.; Weng, J.; Li, J.; Fan, Q.; Zhang, Y.; Ye, D. *Angew. Chem., Int. Ed.* **2019**, *58* (15), 4886–4890.
- (7) Liu, J.; Wu, F.; Wang, M.; Tao, M.; Liu, Z.; Hai, Z. *Anal. Chem.* **2023**, *95* (25), 9404–9408.
- (8) Ye, D.; Shuhendler, A. J.; Cui, L.; Tong, L.; Tee, S. S.; Tikhomirov, G.; Felsher, D. W.; Rao, J. *Nat. Chem.* **2014**, *6* (6), 519–526.
- (9) Huang, R.; Wang, X.; Wang, D.; Liu, F.; Mei, B.; Tang, A.; Jiang, J.; Liang, G. *Anal. Chem.* **2013**, *85* (13), 6203–6207.
- (10) Mizukami, S.; Takikawa, R.; Sugihara, F.; Hori, Y.; Tochio, H.; Wälchli, M.; Shirakawa, M.; Kikuchi, K. *J. Am. Chem. Soc.* **2008**, *130* (3), 794–795.
- (11) Su, H.; Chen, G.; Gangadharmath, U.; Gomez, L. F.; Liang, Q.; Mu, F.; Mocharla, V. P.; Szardenings, A. K.; Walsh, J. C.; Xia, C. F.; Yu, C. *Mol. Imaging Biol.* **2013**, *15* (6), 739–747.
- (12) Freund, P.; Seif, M.; Weiskopf, N.; Friston, K.; Fiehler, M. G.; Thompson, A. J.; Curt, A. *Lancet Neurol.* **2019**, *18* (12), 1123–1135.
- (13) Juweid, M. E.; Mueller, M.; Alhourri, A.; A-Risheq, M. Z.; Mottaghy, F. M. *Cancer* **2021**, *127* (20), 3727–3741.
- (14) Tamaki, N.; Ajmera, V.; Loomba, R. *Nat. Rev. Endocrinol.* **2022**, *18* (1), 55–66.
- (15) Gomes, C. M.; Abrunhosa, A. J.; Ramos, P.; Pauwels, E. K. J. *Adv. Drug Delivery Rev.* **2011**, *63* (7), 547–554.
- (16) Angelovski, G. *Angew. Chem., Int. Ed.* **2016**, *55* (25), 7038–7046.
- (17) Yue, X.; Wang, Z.; Zhu, L.; Wang, Y.; Qian, C.; Ma, Y.; Kiesewetter, D. O.; Niu, G.; Chen, X. *Mol. Pharmaceutics* **2014**, *11* (11), 4208–4217.
- (18) Xie, D.; Yu, M.; Kadakia, R. T.; Que, E. L. *Acc. Chem. Res.* **2020**, *53* (1), 2–10.
- (19) Zhang, C.; Yan, K.; Fu, C.; Peng, H.; Hawker, C. J.; Whittaker, A. K. *Chem. Rev.* **2022**, *122* (1), 167–208.
- (20) Chen, H.; Viel, S.; Ziarelli, F.; Peng, L. *Chem. Soc. Rev.* **2013**, *42* (20), 7971–7982.
- (21) Cosco, D.; Fattal, E.; Fresta, M.; Tsapis, N. *J. Fluorine Chem.* **2015**, *171*, 18–26.
- (22) Janasik, D.; Krawczyk, T. *Chemistry* **2022**, *28* (5), No. e202102556.
- (23) Cametti, M.; Crousse, B.; Metrangolo, P.; Milani, R.; Resnati, G. *Chem. Soc. Rev.* **2012**, *41* (1), 31–42.

- (24) Ahrens, E. T.; Helfer, B. M.; O'Hanlon, C. F.; Schirda, C. *Magn. Reson. Med.* **2014**, *72* (6), 1696–1701.
- (25) Ahrens, E. T.; Zhong, J. *NMR Biomed.* **2013**, *26* (7), 860–871.
- (26) Ruiz-Cabello, J.; Barnett, B. P.; Bottomley, P. A.; Bulte, J. W. M. *NMR Biomed.* **2011**, *24* (2), 114–129.
- (27) Li, S.; Zhang, L.; Xu, Q.; Sui, M.; Xiao, L.; Chen, D.; Jiang, Z.-X.; Zhou, X.; Chen, S. *Adv. Mater.* **2024**, *36* (47), No. 2401513.
- (28) Chen, S.; Xiao, L.; Li, Y.; Qiu, M.; Yuan, Y.; Zhou, R.; Li, C.; Zhang, L.; Jiang, Z.-X.; Liu, M.; Zhou, X. *Angew. Chem., Int. Ed.* **2022**, *61* (50), No. e202213495.
- (29) Bai, H.; Wang, Y.; Hu, Y.; Ye, D. *Biosens. Bioelectron.* **2022**, *216*, No. 114648.
- (30) Weng, J.; Wang, Y.; Zhang, Y.; Ye, D. *J. Am. Chem. Soc.* **2021**, *143* (43), 18294–18304.
- (31) Yan, R.; Hu, Y.; Liu, F.; Wei, S.; Fang, D.; Shuhendler, A. J.; Liu, H.; Chen, H.-Y.; Ye, D. *J. Am. Chem. Soc.* **2019**, *141* (26), 10331–10341.
- (32) Caravan, P.; Ellison, J. J.; McMurry, T. J.; Lauffer, R. B. *Chem. Rev.* **1999**, *99* (9), 2293–2352.
- (33) Li, L.; Chen, C.; Bu, Y.; Wang, J.; Shao, J.; Li, A.; Lin, H.; Gao, J. *Anal. Chem.* **2024**, *96* (26), 10827–10834.
- (34) Li, A.; Luo, X.; Chen, D.; Li, L.; Lin, H.; Gao, J. *Anal. Chem.* **2023**, *95* (1), 70–82.
- (35) Tang, X.; Gong, X.; Ming, J.; Chen, D.; Lin, H.; Gao, J. *Anal. Chem.* **2020**, *92* (24), 16293–16300.
- (36) Yuan, T.; Xu, Y.; Fei, J.; Xue, H.; Li, X.; Wang, C.; Fytas, G.; Li, J. *Angew. Chem., Int. Ed.* **2019**, *58* (32), 11072–11077.
- (37) Bousquet, J. C.; Saini, S.; Stark, D. D.; Hahn, P. F.; Nigam, M.; Wittenberg, J.; Ferrucci, J. T., Jr. *Radiology* **1988**, *166* (3), 693–698.
- (38) Bloembergen, N.; Morgan, L. O. *J. Chem. Phys.* **1961**, *34* (3), 842–850.
- (39) Zhou, Z.; Yang, L.; Gao, J.; Chen, X. *Adv. Mater.* **2019**, *31* (8), No. 1804567.